Research Article | Open Access

Journal of Materials Informatics

Zhang *et al. J. Mater. Inf.* **2026**, *6*, 52 **DOI:**10.20517/jmi.2026.69

Explainable deep learning elucidates orbital–spin synergy in multi-field-responsive Pt-$BiFeO_3$ for efficient photocatalytic H_2 production

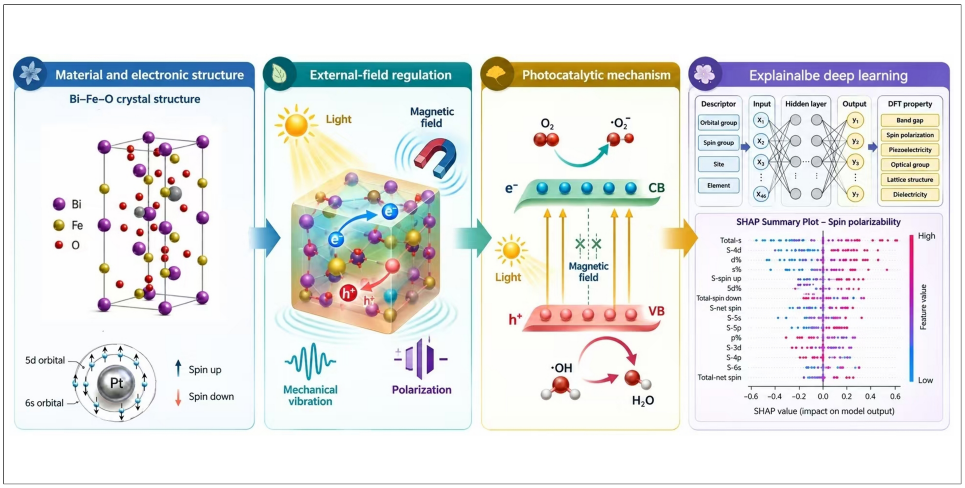
Wanyue Zhang[1], Jianqiao Liu[1,2,*], Lehuan Liang[3], Huixin Guan[1], Peilun Qiu[1], Chuqiao Hu[1], Di Wu[1], Ce Fu[1,*], Qianru Zhang[2,*]

Keywords:
Multifield enhanced photocatalysis, hydrogen production, orbital–spin synergy, Pt-doped $BiFeO_3$, explainable deep learning

Citation: Zhang, W.; Liu, J.; Liang, L.; Guan, H.; Qiu, P.; Hu, C.; Wu, D.; Fu, C.; Zhang, Q. Explainable deep learning elucidates orbital–spin synergy in multi-field-responsive Pt-$BiFeO_3$ for efficient photocatalytic H_2 production. *J. Mater. Inf.* **2026**, *6*, 52. https://dx.doi.org/10.20517/jmi.2026.69

Received: 12 Aug 2026 **First Decision:** 28 Aug 2026 **Revised:** 9 Oct 2026 **Accepted:** 20 Oct 2026 **Published:** 28 Oct 2026

Academic Editor: Hao Li
Copy Editor: Pei-Yun Wang
Production Editor: Pei-Yun Wang



Abstract

Electrons serve as fundamental mediators of energy conversion in photocatalytic systems, governing light harvesting, charge excitation, carrier migration, and surface redox processes that ultimately dictate the efficiency of solar-driven chemical transformations. However, precise manipulation of electronic states in photocatalytic systems remains challenging because the intrinsic complexity of electron configuration and dynamic evolution restricts the optimization of catalytic performance. Herein, we demonstrate that orbital–spin synergy deciphered by explainable deep learning governs multi-field responsiveness of Pt-doped $BiFeO_3$ for efficient photocatalytic hydrogen production. Orbital–spin synergy reconstructs electronic states via Pt 5d–Fe 3d–O 2p hybridization and spin redistribution promoting charge separation across multiple external fields. A multi-property density functional theory database covering 29 transition-metal dopant elements and 58 site-specific $BiFeO_3$ doping configurations was established to screen $BiFeO_3$ using electronic, optical, dielectric, piezoelectric, and spin descriptors. Pt-doped $BiFeO_3$ achieved

[1]College of Information Science and Technology, Dalian Maritime University, Dalian 116026, Liaoning, China.
[2]Institute of Agriculture Resources and Regional Planning, Chinese Academy of Agricultural Sciences, Beijing 100081, China.
[3]Tangshan Kaicheng Electric Control Equipment Group Co., Ltd., Tangshan 063000, Hebei, China.

***Correspondence to:** Prof. Jianqiao Liu, Prof. Ce Fu, College of Information Science and Technology, Dalian Maritime University, Dalian 116026, Liaoning, China. E-mail: jqliu@dlmu.edu.cn; fu_ce@dlmu.edu.cn; Prof. Qianru Zhang, Institute of Agriculture Resources and Regional Planning, Chinese Academy of Agricultural Sciences, Beijing 100081, China. E-mail: zhangqianru@caas.edu.cn

the highest screening score while structural and spectroscopic characterizations confirmed successful Pt incorporation with preserved lattice integrity. Multi-field responsiveness was evaluated through carrier-dynamics measurements and photocatalytic hydrogen evolution under coupled light, magnetic, mechanical, and polarization fields. Suppressed electron–hole recombination affords superior hydrogen evolution activity, prolonged carrier lifetime, reduced charge-transfer resistance, and outstanding cycling stability. This work reveals orbital–spin synergy as an effective pathway for electronic-state engineering, offering new guidance for the development of photocatalytic systems with efficient solar energy conversion.

INTRODUCTION

Electrons serve as the central carriers of energy conversion in photocatalytic systems by coupling photon harvesting with surface redox reactions[1,2]. Electronic excitation determines carrier generation, while carrier migration controls the spatial distribution of reduction and oxidation reactions throughout photocatalytic processes[3]. Electronic interactions regulate energy-level alignment, interfacial charge transfer, and reaction kinetics, thereby dictating solar-to-chemical energy conversion efficiency[4,5]. Despite continuous advances in photocatalyst development, inefficient carrier utilization and severe electron–hole recombination remains major barriers to further performance improvement[6,7]. Conventional optimization strategies mainly adjusted composition, morphology, and heterostructures[8], yet their influence on intrinsic electronic behavior proved limited[9]. Precise regulation of electronic states is accordingly indispensable for reconstructing charge-transfer pathways and improving interfacial redox processes[10]. Advancing photocatalytic solar energy conversion consequently relies increasingly on precise electronic-state engineering[11,12].

Electronic-state engineering emerged as an effective strategy for tailoring carrier dynamics and interfacial charge transfer in photocatalytic systems[13-16]. Band-structure modulation, defect engineering, heterointerface construction, and elemental doping were widely explored to reshape electronic structures and optimize photocatalytic activity[17-24]. These approaches substantially improved light harvesting, charge separation, and reaction kinetics across diverse photocatalytic systems. However, most studies primarily focused on macroscopic electronic characteristics, whereas the microscopic origin of electronic-state evolution remained insufficiently understood. Orbital interaction and spin evolution were commonly investigated as separate phenomena, leaving their intrinsic coupling origin largely unexplored[25-28]. Orbital–spin synergy therefore provides a promising framework for interpreting electronic-state evolution at the atomic scale. This synergistic pathway also establishes a new foundation for precise electronic-state engineering and rational photocatalyst design.

Orbital–spin synergy originated from the intrinsic coupling between orbital hybridization and spin polarization during electronic-state evolution. Orbital hybridization redistributed electron density by modifying orbital overlap and energy-level alignment, which optimized charge-transfer pathways in numerous photocatalytic systems[29-32]. Spin polarization prolonged carrier lifetime by introducing spin-selective transport, thereby suppressing electron–hole recombination during photocatalytic reactions[33-36]. Multiferroic compounds such as $BiFeO_3$ combined visible-light absorption with spontaneous ferroelectric polarization whose internal electric field promoted photogenerated charge separation and enabled polarization-dependent photocatalytic water conversion[37-42]. However, pristine $BiFeO_3$ still suffers from intrinsic limitations, including insufficient electronic-band optimization and rapid recombination of photogenerated charge carriers, which restrict its efficiency for photocatalytic hydrogen evolution. Rational electronic-structure modulation through transition-metal incorporation provides an effective strategy to optimize band-edge characteristics and carrier-transfer behavior. In particular, Pt incorporation is expected to induce orbital reconstruction and spin-related electronic regulation, thereby improving the electronic

conditions required for efficient hydrogen evolution. Electronic redistribution arising from concurrent orbital reconstruction and spin evolution strengthened carrier separation together with interfacial redox activity beyond the capability of independent regulation. These observations indicated that orbital–spin synergy represented the microscopic origin of precise electronic-state engineering rather than two independent electronic effects. Orbital–spin synergy is therefore expected to provide an effective route toward overcoming the intrinsic limitations of electronic-state engineering in photocatalytic systems.

Herein, we develop an integrated computational–experimental framework to decipher orbital–spin synergy in multi-field-responsive Pt-doped $BiFeO_3$ for photocatalytic hydrogen production. A multi-property density functional theory (DFT) database comprising 58 site-specific $BiFeO_3$ doping configurations generated from 29 transition-metal dopant elements at distinct lattice sites is constructed using electronic, optical, dielectric, piezoelectric, and spin descriptors. A unified scoring scheme is applied to rank the candidate systems and identify compositions suitable for subsequent experimental investigation. The selected Pt-doped $BiFeO_3$ is synthesized, followed by structural, morphological, spectroscopic, chemical-state, and ferroelectric characterizations. Photocatalytic hydrogen evolution and carrier dynamics are examined under individual or coupled light, magnetic, mechanical, and polarization fields. Explainable deep learning is combined with electronic-structure calculations to correlate key descriptors with orbital hybridization, spin redistribution, charge migration, and interfacial reaction pathways. This work is expected to establish orbital–spin synergy as a mechanistic basis for electronic-state engineering and guide the development of photocatalytic systems for efficient solar energy conversion.

MATERIALS AND METHODS

Experimental synthesis and evaluation

Pristine and Pt-doped $BiFeO_3$ photocatalysts were synthesized using a modified citrate-assisted sol–gel method. Structural and electronic properties were characterized by X-ray diffraction (XRD), X-ray photoelectron spectroscopy (XPS), and synchrotron X-ray absorption fine structure (XAFS), while X-ray magnetic circular dichroism (XMCD) was employed to probe element-specific spin polarization. Photogenerated carrier dynamics were evaluated by time-resolved photoluminescence (TRPL) and photoelectrochemical measurements. Photocatalytic hydrogen evolution was investigated under simulated solar irradiation alone and under coupled magnetic-field, ferroelectric-polarization, and mechanical-vibration conditions. Full experimental procedures, characterization details, and measurement conditions are provided in the Supplementary Materials.

DFT computational methodology

First-principles calculations were performed to establish the electronic-structure database of transition-metal-modified $BiFeO_3$ and to identify the intrinsic descriptors governing orbital–spin synergy[43-45]. The rhombohedral $BiFeO_3$ structure with an R3c space group and G-type antiferromagnetic ordering was selected as the pristine framework, and its crystal structure is shown in Supplementary Figure 1A. A periodic supercell was constructed based on the experimentally reported lattice configuration to preserve the FeO_6 octahedral connectivity and ferroelectric distortion characteristics of $BiFeO_3$. Transition-metal dopants were introduced by substituting either Bi sites (A sites) or Fe sites (B sites) in the $BiFeO_3$ lattice. A total of 29 candidate transition-metal elements were considered, as shown in Supplementary Figure 1B, and their electronic compatibility with the host lattice was evaluated based on the interaction between dopant d orbitals and the $BiFeO_3$ electronic framework. Pt-doped $BiFeO_3$ was subsequently selected as the representative system for detailed orbital and spin investigation.

All DFT calculations[46-49] were carried out using the projector augmented-wave (PAW) formalism within the generalized gradient approximation (GGA) framework implemented in the Device Studio. The Perdew–Burke–Ernzerhof (PBE) functional was employed to describe exchange–correlation interactions. The

Hubbard U correction was introduced to accurately describe electron localization and magnetic interactions, given the localized nature of Fe 3d and dopant d electrons. Spin-polarized calculations were performed throughout all structural relaxation and electronic-property evaluations to capture the magnetic contribution of transition-metal substitution.

The plane-wave kinetic energy cutoff was set to 500 eV, and Brillouin-zone integration was performed using Monkhorst–Pack k-point meshes with appropriate sampling density. Structural optimization was conducted until the residual forces on each atom were below 0.05 $eV \cdot Å^{-1}$ and the total energy variation reached convergence. The electronic structures, including band structures, density of states (DOS), projected density of states (PDOS), spin density distributions, and charge-density differences, were calculated after structural relaxation using identical computational parameters.

The doped $BiFeO_3$ systems were systematically evaluated using electronic, optical, dielectric, piezoelectric, and spin-related descriptors to construct the multi-property dataset. The band gap, piezoelectric tensor, spin polarization, dielectric constant, and optical properties, including average extinction coefficient, refractive index, reflectance, and absorption coefficient, were extracted from the converged DFT calculations. These descriptors provided a unified computational foundation for subsequent multi-objective screening and explainable deep-learning interpretation of orbital–spin synergy.

Additional calculations incorporating spin-resolved electronic structures were performed for the Pt-doped $BiFeO_3$ system to investigate the hybridization between Pt 5d, Fe 3d, and O 2p orbitals. The orbital-PDOS, differential charge density, electron localization function, and spin-density distribution were analyzed to elucidate the relationship between orbital reconstruction, spin redistribution, and enhanced photocatalytic charge-transfer behavior.

Multi-objective screening

A DFT-driven multi-objective screening strategy[50-54] was established using the calculated properties of transition-metal-doped systems to identify an optimal dopant for regulating the electronic structure and multi-field responsiveness of $BiFeO_3$. Unlike conventional screening approaches relying on a single descriptor, the present strategy simultaneously considered electronic, optical, dielectric, piezoelectric, and spin-related characteristics, aiming to balance visible-light harvesting, carrier separation, internal-field generation, and spin-mediated charge transport.

The calculated transition-metal-doped $BiFeO_3$ systems were first evaluated according to structural stability and electronic compatibility. The formation energy of each doped configuration was calculated to assess the thermodynamic feasibility of dopant incorporation. Systems with unfavorable structural distortion or significant electronic instability were excluded from subsequent comparison. The remaining candidates were quantitatively analyzed using multiple photocatalytic descriptors, including band gap, optical absorption characteristics, dielectric constant, piezoelectric response, and spin polarization.

All selected descriptors were normalized using a min–max scaling approach to enable comparison among different physical quantities. For a given descriptor P_i, the normalized contribution was calculated as:

$$S_i = \frac{P_i - P_{min}}{P_{max} - P_{min}} \times 100$$

where P_{max} and P_{min} represent the maximum and minimum values among all doped configurations. A target-window scoring function was applied to descriptors requiring an optimal range rather than monotonically increasing behavior, such as band gap, to favor photocatalytically suitable electronic structures.

The overall photocatalytic screening score was obtained by averaging the normalized contributions from different performance descriptors:

$$S_{\text{total}} = \frac{1}{5}\sum_{i-1}^{5} S_i$$

where S_i represents the normalized score of each performance descriptor, including the band gap (S_{Eg}), piezoelectric coefficient (S_d), spin polarization ($S\eta$), dielectric constant (S_ε), and optical properties (S_{opt}), Equal weighting was adopted to avoid artificial bias toward any individual property and to evaluate the intrinsic multifunctional capability of each doped system.

Explainable deep-learning framework

An explainable deep-learning framework was established to analyze the nonlinear relationships between multiple DFT-derived descriptors and multiple physical properties relevant to photocatalytic performance, aiming to elucidate the intrinsic origin of the superior photocatalytic performance of Pt-doped $BiFeO_3$. Unlike common data-driven screening strategies that directly predict candidate compositions[55-58], the present framework was designed as a post-screening interpretation model to quantitatively identify the relative contributions of different physical descriptors to the predicted physical properties relevant to catalytic behavior.

The input dataset consisted of the calculated properties of all transition-metal-doped $BiFeO_3$ systems obtained from first-principles calculations. The input features included electronic properties of orbital group and spin group descriptors as well as substitution site and elemental descriptors. Multiple DFT-derived physical properties served as the prediction targets, whereas the comprehensive performance score obtained from the multi-objective screening procedure was used to rank candidates. All descriptors were normalized using min–max scaling prior to model training to eliminate dimensional differences and improve model convergence.

A fully connected deep neural network (DNN)[59-64] was adopted to establish the nonlinear mapping between the descriptor space and the target properties. The network comprised an input layer, multiple hidden layers activated by rectified linear unit (ReLU) functions, and a multi-neuron output layer for multi-target regression. The network parameters were optimized using the Adam optimizer with mean squared error (MSE) as the loss function. To improve model generalization and suppress overfitting caused by the limited dataset size, dropout regularization and early stopping strategies were introduced during training. Five-fold cross-validation was employed to evaluate the predictive performance and robustness of the model. Model performance was quantitatively assessed using the coefficient of determination (R^2), root mean square error (RMSE), and mean absolute error (MAE).

The explainable learning framework provided an interpretable bridge between first-principles calculations and experimental observations[65]. It combined nonlinear prediction capability with feature attribution and enabled the quantitative identification of the electronic and spin-related descriptors governing photocatalytic activity, thereby revealing the orbital–spin synergistic pathway responsible for the enhanced hydrogen evolution performance of Pt-doped $BiFeO_3$. SHapley Additive exPlanations (SHAP)[66-69] were employed to interpret the trained DNN model by quantifying the contribution of each descriptor to each predicted physical property. SHAP was developed based on cooperative game theory and quantified the importance of

Table 1. Multi-objective screening scores of representative single-doped $BiFeO_3$ photocatalysts based on the predicted band gap, piezoelectric tensor, spin polarization, dielectric constant, and optical properties

Sample	Band gap	Piezoelect-ric tensor	Spin polariza-tion	Dielectric constant	Optical properties	Average
$BiFe(Pt)O_3$	90.1	35.8	100.0	47.0	48.0	64.2
$BiFe(Tc)O_3$	87.3	35.1	98.2	41.8	57.4	64.0
$Bi(Ru)FeO_3$	78.1	46.8	79.7	9.5	67.2	56.3
$Bi(Os)FeO_3$	70.2	31.0	84.0	28.7	58.8	54.5
$Bi(Cd)FeO_3$	63.2	100.0	32.9	7.6	66.8	54.1
$BiFe(Zn)O_3$	71.3	27.6	56.6	46.1	56.1	51.5

each input feature by evaluating its marginal contribution to the model output under all possible feature combinations. Both global and local SHAP analyses were performed. Global SHAP values were used to rank the overall importance of different descriptors, whereas local SHAP values were utilized to reveal the dominant factors responsible for the superior performance of Pt-doped $BiFeO_3$.

RESULTS AND DISCUSSION

Multi-objective screening of Pt-doped $BiFeO_3$

A multi-objective screening strategy identifies Pt as the most promising dopant for regulating the electronic properties of $BiFeO_3$ toward efficient photocatalytic hydrogen evolution. Electronic, optical, dielectric, piezoelectric, and spin-related descriptors are integrated into a unified scoring framework to evaluate the overall performance of 58 transition-metal-doped $BiFeO_3$ configurations derived from 29 candidate dopant elements. The comprehensive screening results are summarized in Table 1, where Pt-doped $BiFeO_3$ achieves the highest average score of 64.2 among all candidates. The corresponding raw DFT-calculated physical properties for all 29 dopants are provided in Supplementary Table 1 as the basis for the normalization and screening results presented in Table 1. The superior ranking originates from its balanced performance rather than a single dominant descriptor. Pt substitution reaches the maximum normalized spin polarization score of 100.0 while simultaneously maintaining competitive band-gap, dielectric, piezoelectric, and optical responses. Tc-doped $BiFeO_3$ exhibits a comparable average score of 64.0, yet its lower spin polarization and dielectric response reduce its overall competitiveness. Moreover, despite its competitive theoretical performance, Tc was excluded from further experimental consideration because technetium has no stable isotopes and is intrinsically radioactive, which substantially limits its practical handling and experimental implementation. Therefore, the final selection of Pt was based not only on its comprehensive multi-property performance but also on its greater feasibility for subsequent experimental investigation. These results demonstrate that Pt provides the most favorable balance among multiple functional descriptors, establishing a reliable computational basis for subsequent experimental investigation.

The comparison further indicates that balanced electronic regulation is more critical than maximizing an individual property for photocatalytic systems. Ru-, Os-, and Cd-doped $BiFeO_3$ exhibit excellent performance in specific descriptors but fail to maintain high comprehensive scores because of pronounced trade-offs among different properties. Cd substitution produces the highest piezoelectric response, whereas its weak dielectric response and limited spin polarization substantially reduce the overall evaluation. Ru and Os substitutions enhance optical characteristics but show insufficient dielectric or spin-related performance compared with Pt. The consistently high scores achieved by Pt across all descriptor categories suggest that its electronic configuration simultaneously promotes orbital hybridization and spin polarization, enabling cooperative optimization of multiple physical properties. Such comprehensive superiority distinguishes Pt from conventional dopants selected using single-property criteria. This screening outcome provides the first evidence that Pt is an optimal candidate for constructing orbital–spin synergistic regulation in $BiFeO_3$ and

establishes the foundation for the subsequent structural validation and photocatalytic investigation.

Structural and electronic-state validation of Pt-doped $BiFeO_3$

To clarify the Pt concentration and identify the composition, a Pt-concentration series comprising BFO, 5Pt-BFO, 10Pt-BFO, and 15Pt-BFO was synthesized, where 5, 10, and 15 represent the nominal precursor Pt/Fe molar ratios (%). ICP-OES measurements show actual bulk Pt/Fe molar ratios of 3.31% ± 0.03%, 6.08% ± 0.04%, and 8.21% ± 0.06% for 5Pt-BFO, 10Pt-BFO, and 15Pt-BFO, respectively, as shown in Supplementary Figure 2. As demonstrated by the following photocatalytic measurements, 10Pt-BFO exhibits the optimal performance and is therefore referred to as $BiFe(Pt)O_3$. The incorporation of Pt into the $BiFeO_3$ lattice is confirmed by complementary structural characterization, demonstrating that Pt substitution induces lattice reconstruction rather than surface deposition. XRD patterns in Figure 1A show that all major diffraction peaks remain consistent with the rhombohedral $BiFeO_3$ phase, while slight peak shifts and refined lattice parameters indicate lattice distortion after Pt modification. The concentration-dependent XRD patterns in Supplementary Figure 3 further show that BFO, 5Pt-BFO, 10Pt-BFO, and 15Pt-BFO preserve the characteristic $BiFeO_3$ diffraction pattern without obvious additional reflections. With increasing Pt precursor concentration, the major diffraction doublet shifts downward, consistent with progressive lattice expansion/distortion induced by Pt incorporation. High-resolution transmission electron microscopy in Figure 1B reveals well-resolved lattice fringes without detectable secondary phases, confirming the preservation of high crystallinity. High-angle annular dark-field scanning transmission electron microscopy coupled with elemental mapping in Figure 1C further demonstrates the homogeneous distribution of Bi, Fe, O, and Pt throughout the particles, excluding the formation of Pt-rich aggregates. These structural observations collectively indicate that Pt atoms are potentially incorporated into Fe lattice sites while maintaining the crystalline framework of $BiFeO_3$.

Electronic-state reconstruction associated with Pt incorporation is evidenced by optical and spectroscopic characterization, revealing coordinated modulation of the band structure and local chemical environment. Ultraviolet–visible (UV–Vis) diffuse reflectance spectra and Tauc fitting in Figure 1D demonstrate enhanced visible-light absorption together with a moderate narrowing of the optical band gap, while the calculated band-edge positions remain suitable for photocatalytic hydrogen evolution. Concentration-dependent Tauc plots in Supplementary Figure 4 further reveal progressive band-gap narrowing with increasing Pt precursor concentration, with the optical band gap decreasing from approximately 2.23 eV for BFO to 1.98, 1.84, and 1.64 eV for 5Pt-BFO, 10Pt-BFO, and 15Pt-BFO, respectively. These results demonstrate that Pt concentration systematically modulates the electronic structure of $BiFeO_3$.

High-resolution X-ray photoelectron spectra of Bi 4f and Fe 2p in Figure 1E and F exhibit discernible binding-energy shifts relative to pristine $BiFeO_3$, indicating modified electronic interactions among Bi, Fe, and neighboring atoms after Pt incorporation. Oxygen 1s spectra in Figure 1G reveal changes in lattice oxygen and defect-related oxygen species, suggesting an altered local coordination environment. Pt 4f spectra in Figure 1H verify the existence of chemically incorporated Pt species instead of metallic Pt nanoparticles. Synchrotron Pt L_3-edge X-ray absorption near-edge structure (XANES) and Fourier-transform extended X-ray absorption fine structure (FT-EXAFS) further provide direct local-structure evidence for Pt-centered electronic reconstruction. As shown in Figure 1I, the absorption-edge position and white-line intensity of $BiFe(Pt)O_3$ lie between those of Pt foil and PtO_2, indicating that Pt exists as chemically incorporated positively charged species rather than metallic Pt. In Figure 1J, the dominant FT-EXAFS peak of Pt-modified $BiFeO_3$ appears at ~1.63 Å, close to the first-shell feature of PtO_2 (~1.71 Å) and distinctly different from the Pt–Pt coordination peak of Pt foil (~2.64 Å), indicating that Pt is mainly coordinated with O instead of forming metallic Pt aggregates. The EXAFS fitting in Figure 1K reproduces the experimental spectrum well with a small residual, supporting the Pt–O-dominated local coordination environment and

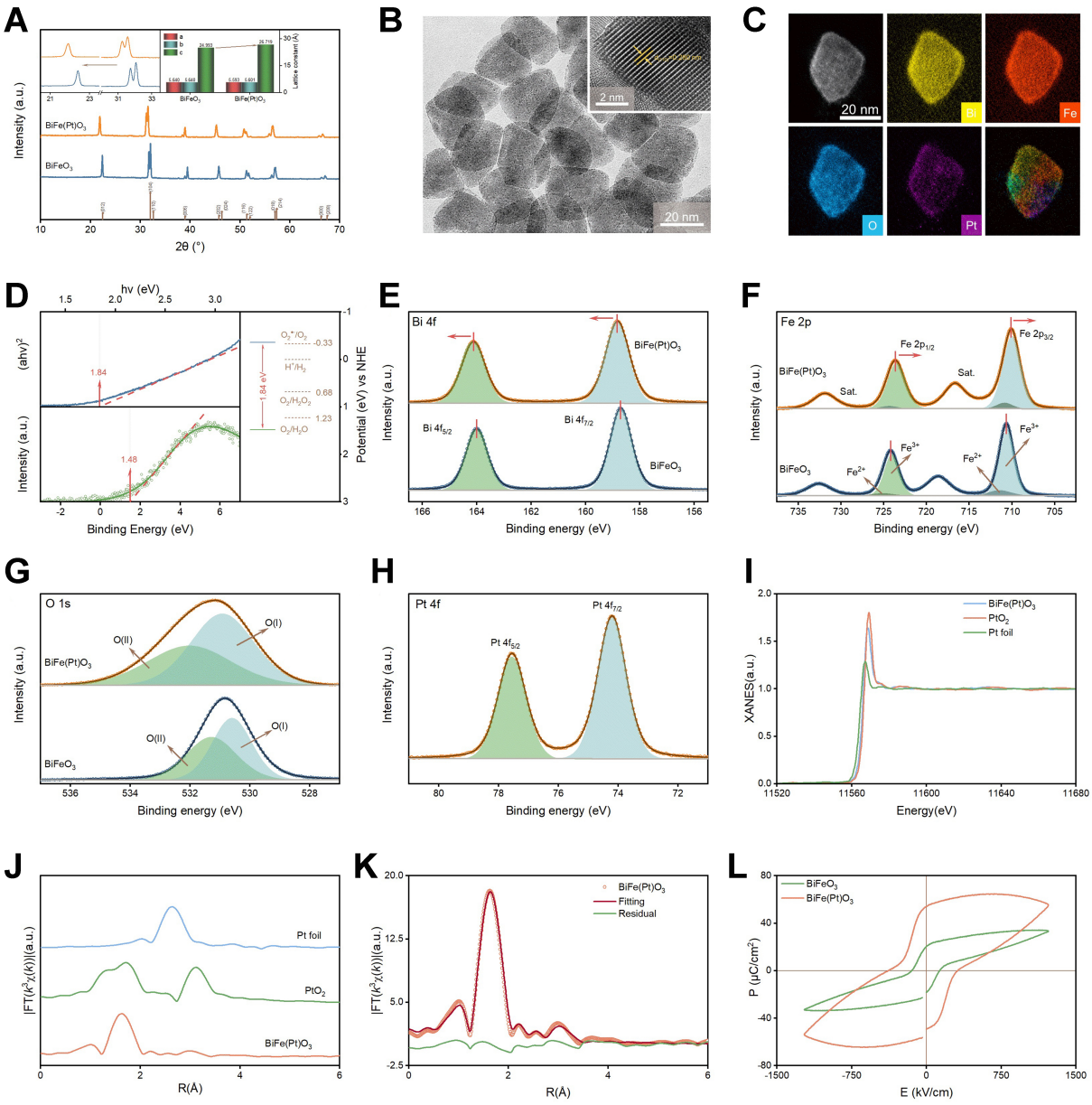


Figure 1. Experimental characterization of pristine $BiFeO_3$ and $BiFe(Pt)O_3$ photocatalysts: (A) XRD patterns with enlarged diffraction peaks and corresponding lattice parameters; (B) TEM image and HRTEM image of the $BiFe(Pt)O_3$ sample; (C) HAADF-STEM elemental mapping images of Bi, Fe, O, and Pt; (D) UV–Vis diffuse reflectance spectra and corresponding Tauc plots together with the calculated band-edge positions; (E) High-resolution XPS spectra of Bi 4f; (F) High-resolution XPS spectra of Fe 2p; (G) High-resolution XPS spectra of O 1s; (H) High-resolution XPS spectra of Pt 4f; (I) Pt L_3-edge XANES spectra of $BiFe(Pt)O_3$ together with PtO_2 and Pt foil references; (J) Pt L_3-edge FT-EXAFS spectra of Pt-modified $BiFeO_3$, PtO_2, and Pt foil; (K) R-space EXAFS fitting of Pt-modified $BiFeO_3$; (L) Ferroelectric hysteresis (P–E) loops of pristine $BiFeO_3$ and $BiFe(Pt)O_3$. XRD: X-ray diffraction; TEM: transmission electron microscopy; HRTEM: high-resolution transmission electron microscopy; HAADF-STEM: high-angle annular dark-field scanning transmission electron microscopy; UV–Vis: ultraviolet–visible; XPS: X-ray photoelectron spectroscopy; XANES: X-ray absorption near-edge structure; FT-EXAFS: Fourier-transform extended X-ray absorption fine structure.

providing direct experimental support for the Pt-centered local structural/electronic reconstruction associated with the Pt 5d–Fe 3d–O 2p hybridization revealed by DFT. These results consistently demonstrate that Pt substitution reconstructs the electronic environment of $BiFeO_3$ rather than introducing isolated surface species.

Ferroelectric polarization is simultaneously reinforced after Pt substitution, providing additional driving force for charge separation during photocatalysis. Polarization–electric field hysteresis loops in Figure 1L exhibit an enlarged polarization response for $BiFe(Pt)O_3$ compared with pristine $BiFeO_3$, indicating strengthened spontaneous polarization and improved ferroelectric behavior. Enhanced polarization increases the internal electric field, which facilitates directional migration of photogenerated electrons and holes while suppressing carrier recombination. The coexistence of lattice reconstruction, electronic-state modulation, and strengthened ferroelectric polarization establishes a synergistically optimized electronic framework. These structural and electronic characteristics provide direct experimental evidence supporting the computational screening results and create favorable conditions for the enhanced multi-field-responsive photocatalytic hydrogen evolution discussed in the following section.

Multi-field-responsive photocatalytic hydrogen evolution

$BiFe(Pt)O_3$ exhibits substantially enhanced photocatalytic hydrogen evolution, and the improvement becomes more pronounced under coupled external fields. Hydrogen evolution rates under different reaction conditions are compared in Figure 2A, where pristine $BiFeO_3$ shows limited activity in both pure H_2O and H_2O/MeOH solutions. Pt substitution markedly increases hydrogen production under light irradiation, confirming the effectiveness of electronic-state regulation in promoting photocatalytic activity. Additional magnetic, electric polarization, and ultrasonic fields further increase the hydrogen evolution rate, while the simultaneous implementation of multiple external fields produces the highest catalytic performance. The enhancement is consistently observed in both reaction media, indicating that the cooperative effect is not restricted to a specific solution environment. These results demonstrate that Pt substitution and multi-field coupling operate synergistically to maximize photocatalytic hydrogen evolution.

The Pt-concentration dependence was further examined under L and L + M conditions [Supplementary Figure 5]. Among the investigated compositions, 10Pt-BFO exhibits the highest H_2 evolution rates of 246.8 ± 9.7 $\mu mol \cdot g^{-1} \cdot h^{-1}$ under L and 628.3 ± 18.4 $\mu mol \cdot g^{-1} \cdot h^{-1}$ under L + M, whereas further increasing the nominal Pt/Fe ratio to 15% decreases the corresponding rates to 191.6 ± 8.5 and 398.7 ± 14.9 $\mu mol \cdot g^{-1} \cdot h^{-1}$, respectively. The magnetic-field-induced enhancement increases from 34.6% for BFO to 90.4% for 5Pt-BFO and reaches a maximum of 154.6% for 10Pt-BFO before decreasing to 108.1% for 15Pt-BFO. Therefore, 10Pt-BFO is identified as the optimal composition among the Pt concentrations investigated in this work. Together with the element-specific XMCD evidence obtained for 10Pt-BFO, this concentration-dependent magnetic response supports the modulation of the orbital–spin-related electronic response by Pt concentration.

To exclude a dominant contribution from nonspecific magnetic-field-induced solution convection or mass-transport enhancement, a non-magnetic counterpart catalyst, Zn_2SnO_4, was further examined under identical photocatalytic conditions, as shown in Supplementary Figure 6. Zn_2SnO_4 exhibits only a marginal change in the H_2 evolution rate from 88.6 ± 4.3 to 90.1 ± 4.6 $\mu mol \cdot g^{-1} \cdot h^{-1}$ upon applying the magnetic field, whereas $BiFe(Pt)O_3$ increases markedly from 246.8 ± 9.7 to 628.3 ± 18.4 $\mu mol \cdot g^{-1} \cdot h^{-1}$ under the same comparison. This control result rules out a dominant contribution from nonspecific bulk mass-transport effects and supports a catalyst-specific magnetic/spin-related contribution to the magnetic-field enhancement observed for $BiFe(Pt)O_3$. These results, together with the non-magnetic control experiment, demonstrate that Pt substitution and multi-field coupling operate synergistically to maximize photocatalytic hydrogen evolution, with the magnetic-field contribution mainly arising from catalyst-specific magnetic/spin-related regulation rather than nonspecific bulk mass-transport effects.

The superior hydrogen evolution performance is accompanied by a significant improvement in photon utilization efficiency under multi-field regulation. Apparent quantum yields measured at 420 nm are summarized in Figure 2B, showing that $BiFe(Pt)O_3$ consistently achieves higher AQY values than pristine

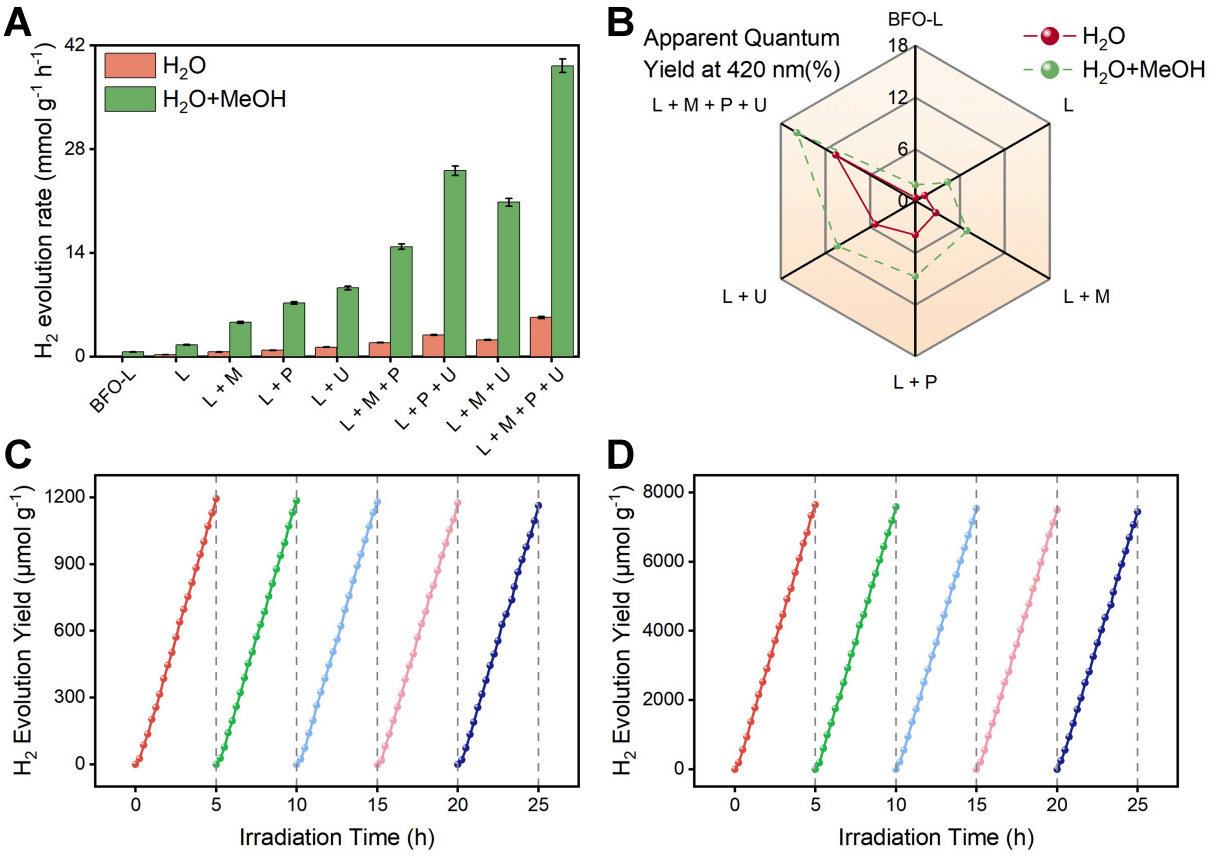


Figure 2. Photocatalytic hydrogen evolution performance of pristine $BiFeO_3$ and multi-field-assisted $BiFeO_3$ photocatalysts: (A) H_2 evolution rates of pristine $BiFeO_3$ under light irradiation (BFO-L) and Pt-doped $BiFeO_3$ under different combinations of light irradiation (L), magnetic field (M), electric polarization (P), and ultrasonic vibration (U), measured in pure H_2O and H_2O/MeOH solutions; (B) AQYs at 420 nm of different multi-field-assisted photocatalytic systems under H_2O and H_2O/MeOH solutions; (C) Cycling stability of photocatalytic H_2 evolution under light irradiation in pure H_2O without external field; (D) Cycling stability of photocatalytic H_2 evolution under light irradiation in H_2O/MeOH solution without external field. The different colored segments represent independent hydrogen production cycles. After each 5-hour irradiation, the reaction system was evacuated and purged with gas before starting the next cycle. AQYs: Apparent quantum yields.

$BiFeO_3$ under identical irradiation conditions. Coupled external fields further increase the AQY in both pure H_2O and H_2O/MeOH systems, indicating that a larger proportion of incident photons is effectively converted into chemical energy. The performance enhancement follows the same trend as the hydrogen evolution rate, confirming the strong correlation between catalytic activity and photon conversion efficiency. Higher AQY values also suggest that the coupled-field strategy improves the utilization of photogenerated charge carriers rather than merely increasing the reaction rate. These observations verify that the multi-field-responsive photocatalytic system achieves efficient solar-energy conversion through cooperative regulation. To further evaluate the overall solar-energy conversion performance, the solar-to-hydrogen (STH) conversion efficiency was calculated under the optimal multi-field condition. In pure H_2O, $BiFe(Pt)O_3$ achieves an STH efficiency of 0.533%. For the H_2O/MeOH system, in which methanol serves as a sacrificial reagent, the corresponding apparent STH efficiency reaches 3.96%. The AQY at 420 nm therefore characterizes the wavelength-specific photon utilization efficiency, whereas the STH value provides a complementary measure of the overall energy-conversion performance under the applied irradiation conditions. To further benchmark the hydrogen-evolution performance of the present system against representative $BiFeO_3$-based photocatalysts, a comparison of reported H_2 evolution rates is provided in Supplementary Table 2. Although the experimental conditions differ among the reported studies, the comparison indicates that $BiFe(Pt)O_3$ exhibits competitive hydrogen-evolution performance, particularly under multi-field coupling, highlighting the effectiveness of

combining Pt-induced electronic-state regulation with external-field modulation.

The photocatalytic activity is maintained during repeated operation, confirming the robustness of the $BiFe(Pt)O_3$ photocatalyst. Cycling tests performed in pure H_2O and H_2O/MeOH solutions without external fields are presented in Figure 2C and D, respectively. Stable hydrogen evolution rates are preserved throughout consecutive individual reaction cycles without noticeable performance decay in either reaction medium. To evaluate cycling stability metrics, the H_2 evolution yield obtained in each cycle was compared with that of the first cycle. After the fifth cycle, the H_2 evolution yield maintains 97.40% in pure H_2O and 97.44% in H_2O/MeOH solution, respectively. The absence of obvious deactivation indicates that Pt substitution does not compromise the structural integrity or catalytic durability of $BiFeO_3$ during prolonged photocatalysis. Consistent catalytic stability under different reaction environments further demonstrates the reliability of the multi-field-responsive system for long-term operation. These results establish that $BiFe(Pt)O_3$ simultaneously achieves high activity, high photon utilization efficiency, and excellent operational stability, providing a solid experimental foundation for the subsequent investigation of charge-transfer dynamics.

Charge-transfer dynamics and reactive-species evolution

Efficient separation and prolonged lifetime of photogenerated charge carriers are achieved after Pt substitution, providing the fundamental origin of the enhanced photocatalytic activity. TRPL spectroscopy is employed to evaluate carrier recombination dynamics, while electrochemical impedance spectroscopy (EIS) is used to characterize interfacial charge-transfer resistance. Decay curves in Figure 3A exhibit a slower photoluminescence decay for $BiFe(Pt)O_3$ than for pristine $BiFeO_3$, indicating a prolonged carrier lifetime and suppressed radiative recombination. The steady-state photoluminescence spectra in Supplementary Figure 7 show distinct PL characteristics for pristine $BiFeO_3$ and $BiFe(Pt)O_3$, further demonstrating that Pt incorporation effectively modulates the recombination behavior of photogenerated charge carriers. Nyquist plots in Figure 3B display a significantly reduced semicircle diameter after Pt incorporation, demonstrating lower charge-transfer resistance at the electrode–electrolyte interface. Bode phase fitting in Figure 3C further reveals an extended electron lifetime, consistent with the impedance results and the photoluminescence measurements. The corresponding frequency-dependent electrochemical response shown in Supplementary Figure 8 further distinguishes pristine $BiFeO_3$ from $BiFe(Pt)O_3$, providing additional evidence for the Pt-induced regulation of interfacial charge-transfer kinetics. These observations suggest that Pt substitution facilitates carrier separation and interfacial charge transport, establishing favorable electronic conditions for efficient photocatalysis.

Charge migration is further strengthened under coupled external fields, demonstrating that the multi-field strategy actively regulates carrier transport rather than merely enhancing catalytic output. Transient photocurrent measurements are conducted to evaluate the separation and migration efficiency of photogenerated charge carriers under different operating conditions. Photocurrent responses in Figure 3D show that $BiFe(Pt)O_3$ produces a considerably higher photocurrent than pristine $BiFeO_3$ under light irradiation, reflecting more efficient carrier extraction. The photocurrent responses in Figure 3E further reveal enhancements in photocurrent under different multi-field-assisted conditions. The highest photocurrent is obtained when all external fields are simultaneously applied, suggesting more efficient charge separation and migration under the coupled-field conditions. To further clarify the individual contributions of the external fields, dark transient photocurrent measurements were performed for pristine $BiFeO_3$. As shown in Supplementary Figure 9A, the photocurrent response varies with magnetic-field strength, while Supplementary Figure 9B shows the corresponding response under different ultrasonic powers. In addition, Supplementary Figure 9C compares the transient photocurrent responses of prepoled, unpoled, and reverse-poled $BiFeO_3$, revealing the influence of the ferroelectric polarization state on field-induced charge migration

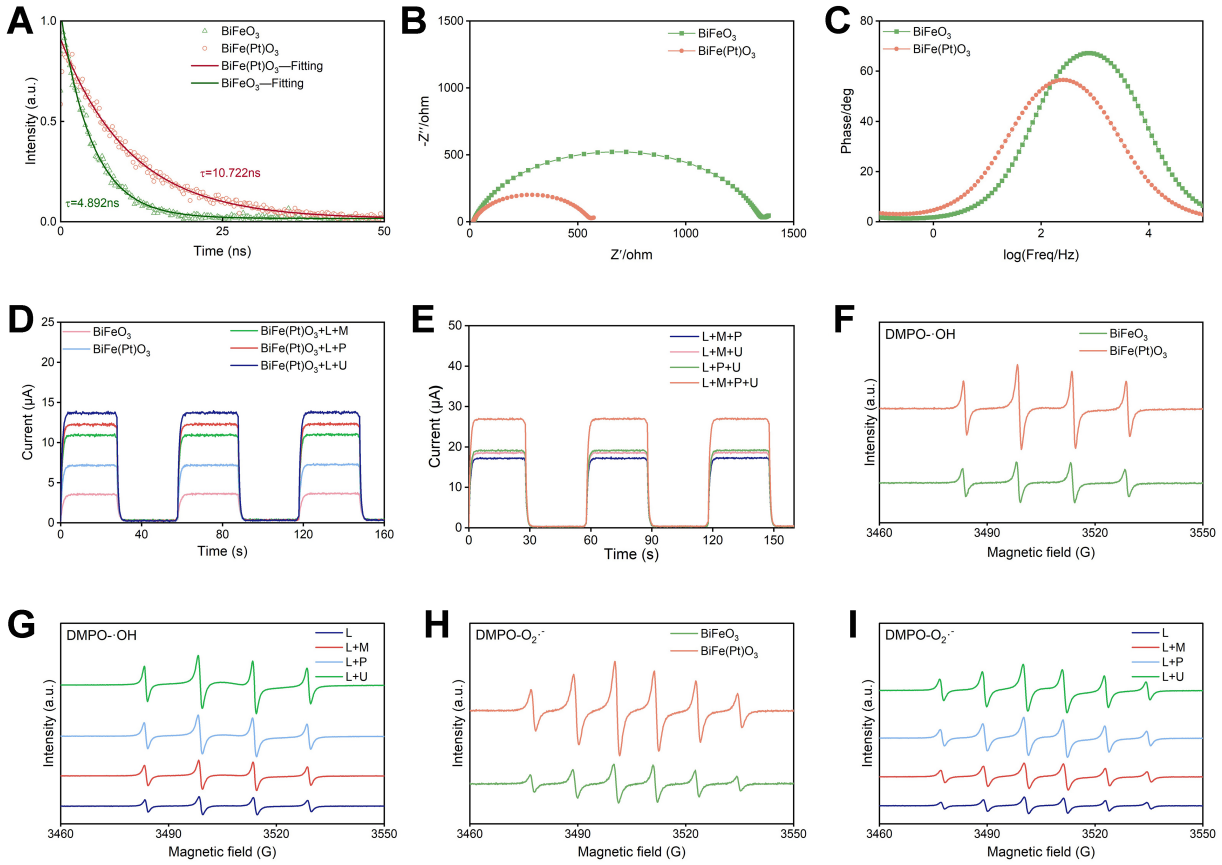


Figure 3. Photoelectrochemical properties and reactive oxygen species characterization of pristine $BiFeO_3$ and $BiFe(Pt)O_3$ photocatalysts: (A) TRPL decay spectra; (B) EIS Nyquist plots; (C) Bode phase plots; (D) Transient photocurrent responses of pristine $BiFeO_3$, and $BiFe(Pt)O_3$ under light irradiation (L) with individual external field of magnetic field (M), electric polarization (P), or ultrasonic vibration (U); (E) Transient photocurrent responses of $BiFe(Pt)O_3$ under different multi-field-assisted conditions; (F) ESR spectra of DMPO–•OH for pristine $BiFeO_3$ and $BiFe(Pt)O_3$ under light irradiation; (G) ESR spectra of DMPO–•OH for $BiFe(Pt)O_3$ under different multi-field-assisted conditions; (H) ESR spectra of DMPO–$•O_2^-$ for pristine $BiFeO_3$ and $BiFe(Pt)O_3$ under light irradiation; (I) ESR spectra of DMPO–$•O_2^-$ for $BiFe(Pt)O_3$ under different multi-field-assisted conditions. TRPL: Time-resolved photoluminescence; EIS: electrochemical impedance spectroscopy; ESR: electron spin resonance; DMPO: 5,5-dimethyl-1-pyrroline N-oxide.

even in the absence of light irradiation. To quantitatively distinguish the synergistic enhancement from a simple additive effect of individual external fields, synergistic factors were calculated for both dual-field and triple-field coupling conditions. For the pristine reaction system, the synergistic factors of magnetic–polarization (M + P), polarization–ultrasonic (P + U), and magnetic–ultrasonic (M + U) coupling are 1.68, 1.64, and 1.42, respectively, while the triple-field coupling exhibits a significantly higher synergistic factor of 2.51. In the methanol-assisted system, the corresponding dual-field synergistic factors are 1.52, 1.76, and 1.79, respectively, and the triple-field coupling reaches 2.30. All synergistic factors are higher than unity, indicating that the enhanced photocatalytic response originates from cooperative interactions among the coupled fields rather than a simple superposition of individual field effects. These results demonstrate that coupled external fields cooperate with Pt-induced electronic-state regulation to maximize charge-transfer efficiency. Together with the negligible magnetic-field response of the non-magnetic Zn_2SnO_4 control photocatalyst in photocatalytic H_2 evolution shown in Supplementary Figure 6, they further indicate that the magnetic-field enhancement observed for $BiFe(Pt)O_3$ does not mainly originate from nonspecific solution convection or bulk mass-transport effects.

Reactive oxygen species generated during photocatalysis are markedly promoted after Pt substitution, indicating more efficient utilization of photogenerated carriers in surface redox reactions. Electron spin

resonance (ESR) spectroscopy is performed to detect hydroxyl radicals (•OH) and superoxide radicals ($•O_2^-$), providing direct evidence for photocatalytic reaction intermediates. Spectra in Figure 3F show that $BiFe(Pt)O_3$ generates stronger 5,5-dimethyl-1-pyrroline N-oxide (DMPO)–•OH signals than pristine $BiFeO_3$ under light irradiation, suggesting enhanced hydroxyl radical generation. Signal intensities further increase under coupled external fields, as illustrated in Figure 3G, confirming that multi-field regulation promotes hydroxyl radical generation. Comparable behavior is observed for superoxide radicals, where Figure 3H and I display significantly enhanced DMPO–$•O_2^-$ signals after Pt substitution and further amplification under multi-field conditions. Additional ESR measurements under dark and individual external-field conditions further clarify the field-dependent generation of reactive species. Supplementary Figure 10A and B compare the DMPO–•OH signals of pristine $BiFeO_3$ and $BiFe(Pt)O_3$, respectively, under dark, magnetic-field, electric-polarization, and ultrasonic-vibration conditions. Correspondingly, Supplementary Figure 10C and D present the DMPO–$•O_2^-$ signals of pristine $BiFeO_3$ and $BiFe(Pt)O_3$ under the same conditions. These results provide complementary evidence for the regulation of both hydroxyl- and superoxide-radical generation by the external fields and Pt modification. These ESR results suggest that the improved carrier dynamics are associated with enhanced generation of reactive species during photocatalysis.

Charge-transfer regulation, carrier utilization, and reactive-species generation operate cooperatively to explain the superior photocatalytic hydrogen evolution of $BiFe(Pt)O_3$. Spectroscopic and electrochemical characterization consistently demonstrate prolonged carrier lifetime, accelerated charge migration, and reduced recombination after Pt substitution. Multi-field coupling further strengthens these processes by enhancing carrier transport and increasing the generation of reactive intermediates. Strong agreement between the carrier-dynamics measurements and the photocatalytic performance establishes a clear structure–property relationship. These experimental observations are consistent with the proposed orbital–spin synergistic regulation and provide supporting evidence for the descriptor interpretation presented in the following explainable deep-learning investigation.

Explainable deep-learning interpretation of orbital–spin descriptors

An explainable deep-learning framework successfully establishes the quantitative relationship between orbital–spin descriptors and the functional properties of $BiFe(Pt)O_3$. A DNN combined with SHAP is constructed to identify the dominant physical descriptors governing photocatalytic behavior. The workflow illustrated in Figure 4A integrates orbital configuration, spin characteristics, substitution-site information, and elemental descriptors into a unified prediction framework for band gap, piezoelectric response, and spin polarization. Computational descriptors derived from DFT calculations are incorporated into the learning process to capture the nonlinear interactions among different physical parameters. Explainable feature attribution enables direct interpretation of descriptor contributions rather than treating the prediction model as a black box. This framework provides a quantitative platform for revealing the intrinsic electronic factors responsible for the superior photocatalytic performance of $BiFe(Pt)O_3$.

Prediction results demonstrate that the trained deep-learning model can effectively reproduce the key functional properties of transition-metal-doped $BiFeO_3$. The DNN model was constructed using orbital-, spin-, substitution-site-, and elemental descriptors as input features. Five-fold cross-validation was employed to evaluate the predictive capability and generalization performance of the model. All prediction results shown in Figure 4B-D were obtained using the same DNN architecture and training strategy described in the Methods section. The SHAP contributions in Figure 4E-G were further calculated using this trained DNN model, ensuring consistency between the prediction and interpretability. For band-gap prediction, the out-of-fold predictions showed good agreement with the DFT-calculated values [Figure 4B], yielding an R^2 of 0.8268, an MAE of 0.1501, and an RMSE of 0.2035. Similarly, the model achieved an R^2 of 0.7901, an MAE of 0.0762, and an RMSE of 0.1016 for the piezoelectric tensor [Figure 4C]. For spin polarization, an R^2 of 0.8113,

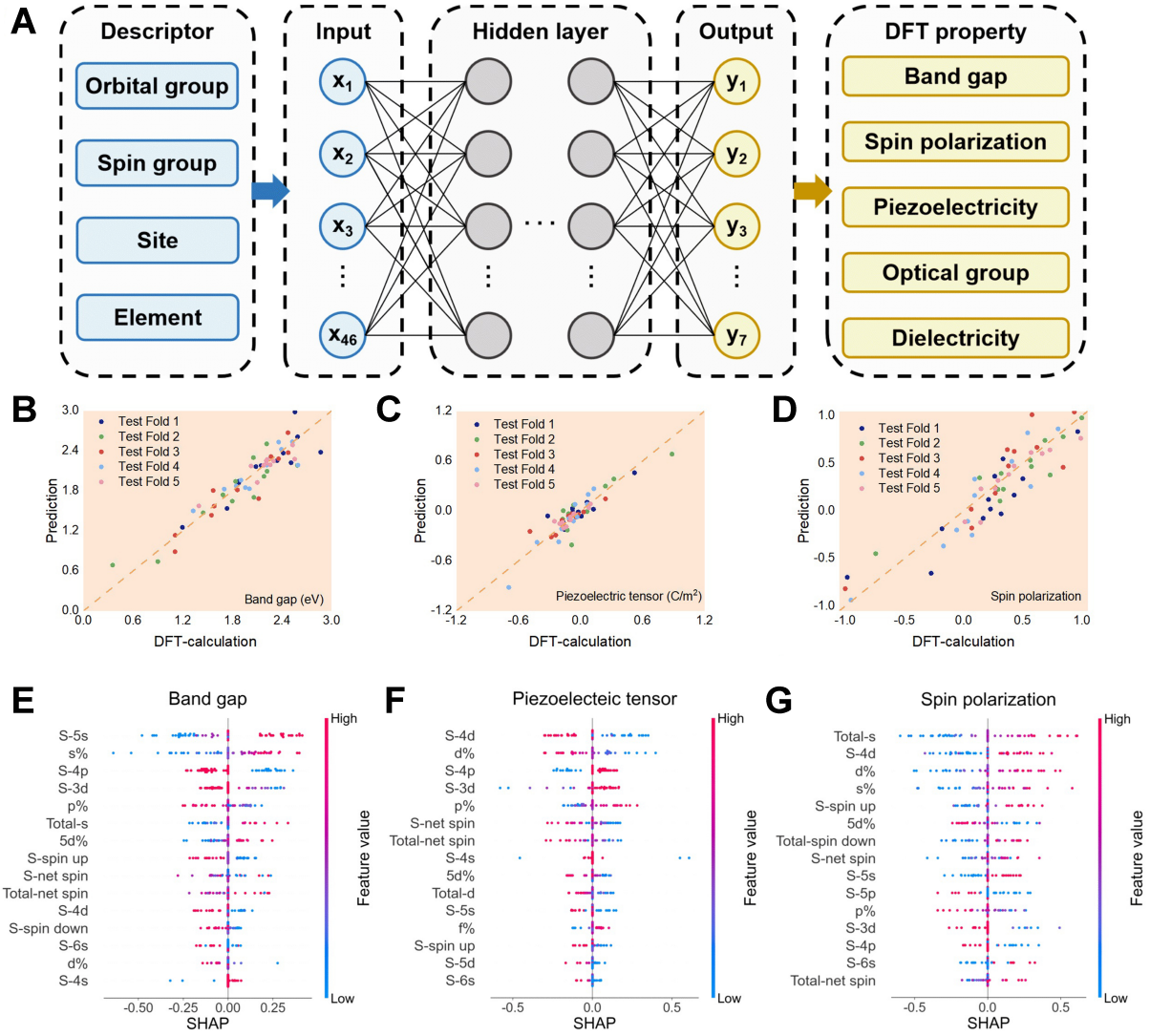


Figure 4. Machine learning framework and feature interpretation for predicting the properties of $BiFeO_3$-based materials: (A) Schematic illustration of the machine learning workflow for predicting material properties based on orbital, spin, site, and elemental descriptors; (B) Comparison between the predicted and DFT-calculated band gaps obtained by five-fold cross-validation; (C) Comparison between the predicted and DFT-calculated piezoelectric tensors obtained by five-fold cross-validation; (D) Comparison between the predicted and DFT-calculated spin polarizations obtained by five-fold cross-validation; (E) SHAP summary plot illustrating the feature importance for band gap prediction; (F) SHAP summary plot illustrating the feature importance for piezoelectric tensor prediction; (G) SHAP summary plot illustrating the feature importance for spin polarization prediction. DFT: Density functional theory; SHAP: SHapley Additive exPlanations.

an MAE of 0.1560, and an RMSE of 0.1923 were obtained [Figure 4D]. The consistently high predictive performance across these distinct physical properties confirms that the model effectively captures the nonlinear relationships among orbital, spin, structural, and elemental descriptors. These results establish the reliability of the explainable deep-learning framework and provide a robust basis for subsequent descriptor interpretation.

Feature-attribution examination reveals that orbital and spin descriptors dominate the prediction of photocatalytic-related properties. The definitions and physical meanings of the key descriptors adopted as input features for SHAP interpretability are summarized in Supplementary Table 3. SHAP investigation is performed to quantify the contribution of individual descriptors to each predicted property and to identify

the governing physical factors. The SHAP summary plot for band-gap prediction in Figure 4E highlights the leading descriptors responsible for electronic-structure regulation. Descriptor importance for the piezoelectric tensor is summarized in Figure 4F, demonstrating that lattice-related and electronic descriptors jointly influence polarization behavior. The SHAP distribution for spin polarization in Figure 4G identifies spin-associated descriptors as the primary contributors to magnetic characteristics, while orbital descriptors provide complementary regulation through electronic hybridization. These findings demonstrate that orbital configuration and spin characteristics cooperate to control the key functional properties relevant to photocatalytic hydrogen evolution.

Explainable deep learning provides quantitative evidence linking descriptor importance to the enhanced photocatalytic performance of $BiFe(Pt)O_3$. Accurate prediction and interpretable feature attribution consistently identify orbital–spin descriptors as the dominant variables governing electronic regulation. The identified descriptor hierarchy indicates that the enhanced photocatalytic performance is closely associated with specific orbital–spin characteristics rather than being determined by a single structural parameter. Quantitative interpretation of these descriptor contributions further links the data-driven analysis to the underlying electronic-structure features. These results provide a rational basis for further examining the electronic origin of the enhanced photocatalytic performance and naturally motivate the DFT investigation presented in the following section.

Orbital–spin synergy in electronic-state reconstruction

First-principles calculations guided by explainable machine learning reveal that orbital occupation and net spin jointly determine the electronic-state reconstruction responsible for the superior photocatalytic performance of $BiFe(Pt)O_3$. DFT is employed to establish quantitative relationships between electronic descriptors and functional properties, while machine-learning interpretation is used to identify the governing variables. Orbital electron distributions and net-spin variations for elemental substitution at the A and B sites are summarized in Figure 5A, demonstrating systematic evolution of the electronic configuration after substitution. Correlation examination in Figure 5B shows that the fraction of 5d electrons exhibits a clear relationship with the predicted band gap, piezoelectric tensor, and spin polarization, indicating that orbital occupation simultaneously regulates multiple functional properties. Comparable trends are observed for the net spin in Figure 5C, confirming that spin regulation cooperates with orbital reconstruction rather than acting independently. The three-dimensional descriptor map in Figure 5D further illustrates the coupled relationship among band gap, piezoelectric response, and spin polarization across different substitution systems, providing quantitative evidence that orbital and spin descriptors constitute the fundamental driving forces for electronic-state reconstruction. These results establish a general descriptor-level origin explaining why Pt achieves the most balanced multifunctional regulation among all transition-metal dopants.

Electronic-structure calculations for the representative $BiFe(Pt)O_3$ system directly demonstrate the microscopic origin of orbital–spin synergistic regulation. Total and partial density-of-states calculations are performed to analyze the redistribution of electronic states near the Fermi level and the hybridization among different atomic orbitals. The total density of states (TDOS) presented in Figure 6A reveals that Pt substitution reconstructs the electronic states surrounding the Fermi level while preserving the semiconducting character required for photocatalysis. Partial density-of-states examination in Figure 6B shows pronounced hybridization among Pt 5d, Fe 3d, and O 2p orbitals, consistent with the Pt-centered local structural/electronic reconstruction evidenced by Pt L_3-edge XANES and FT-EXAFS, and indicating strengthened electronic coupling within the crystal lattice. Charge redistribution further confirms that orbital–spin synergistic regulation extends from local electronic reconstruction to the overall photocatalytic process. Charge-density calculations are conducted to visualize the spatial redistribution of electrons induced by Pt substitution and to clarify its influence on carrier migration. Charge-density distributions in Figure 6C

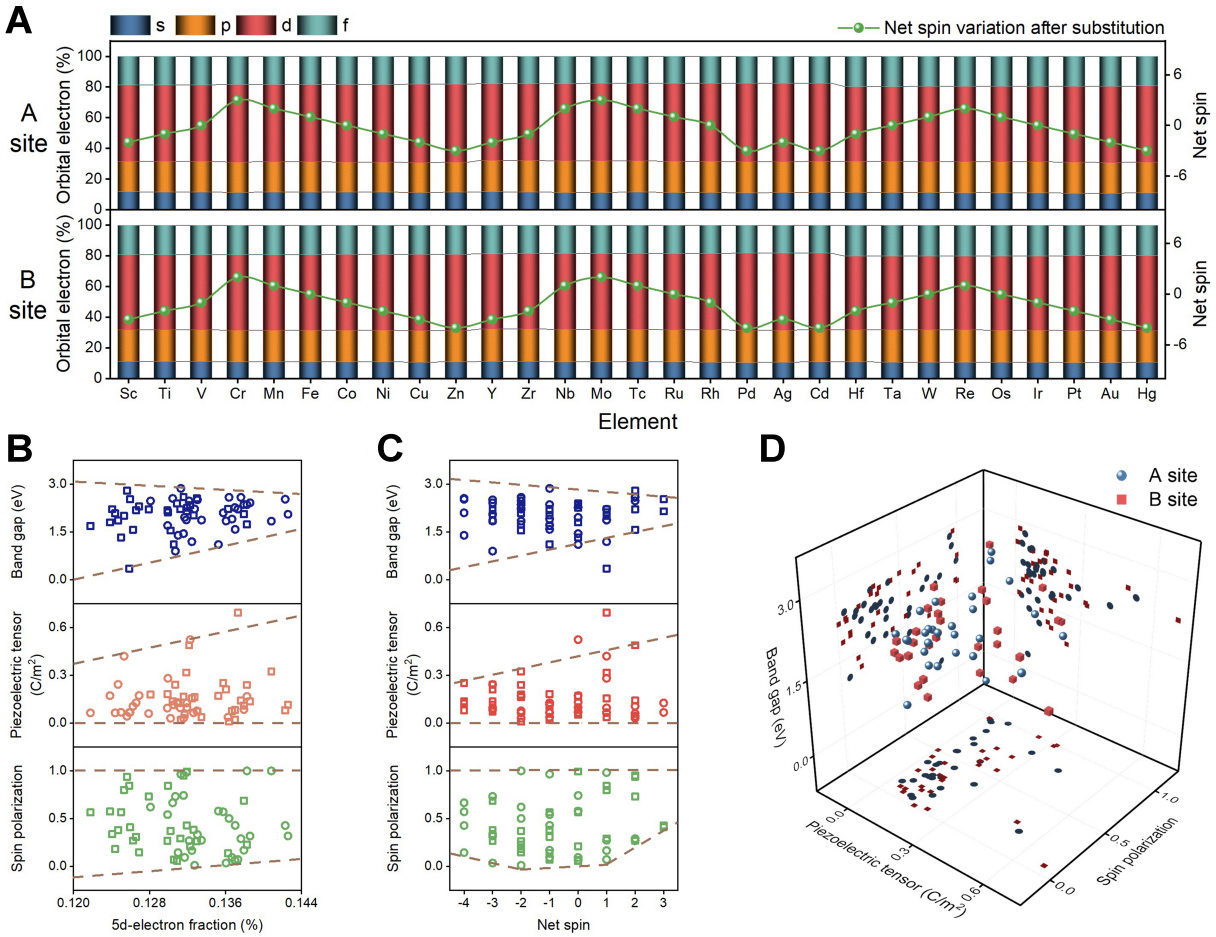


Figure 5. Machine learning-guided examination of elemental substitution effects on the electronic structure and functional properties of $BiFeO_3$: (A) Orbital electron distributions and net spin variations induced by elemental substitution at the A and B sites; (B) Correlations between the 5d-electron fraction and the predicted band gap, piezoelectric tensor, and spin polarization; (C) Correlations between the net spin and the predicted band gap, piezoelectric tensor, and spin polarization; (D) Three-dimensional relationship among the predicted band gap, piezoelectric tensor, and spin polarization for elemental substitutions at the A and B sites.

exhibit pronounced electron accumulation and depletion around the Pt-centered coordination environment, indicating enhanced electronic interaction and directional charge transfer between neighboring atoms. Direct experimental evidence for Pt-induced atomic-scale spin redistribution is further provided by element-specific X-ray absorption spectroscopy (XAS)/XMCD measurements. As shown in Figure 6D, both pristine $BiFeO_3$ and $BiFe(Pt)O_3$ exhibit characteristic Fe $L_{2,3}$-edge XAS features, whereas the XMCD response becomes markedly stronger after Pt substitution. Specifically, the peak-to-peak Fe XMCD amplitude increases from 0.0050 for pristine $BiFeO_3$ to 0.0088 for $BiFe(Pt)O_3$, indicating enhanced Fe-centered spin polarization. Moreover, distinct Pt $L_{2,3}$-edge XMCD signals are observed for $BiFe(Pt)O_3$ in Figure 6E, with peak-to-peak amplitudes of 0.0036 at the Pt L_3 edge and 0.0030 at the Pt L_2 edge, directly evidencing spin-polarized Pt 5d states. These XMCD results experimentally confirm that Pt substitution induces simultaneous Pt-centered magnetic polarization and Fe-centered spin redistribution, in good agreement with the DFT-predicted orbital–spin synergy. Enhanced orbital overlap promotes charge delocalization and modifies the electronic transition pathway, providing a microscopic explanation for the experimentally observed band-structure regulation and improved carrier transport. These electronic-structure characteristics demonstrate that Pt substitution simultaneously optimizes orbital hybridization and spin-related electronic interactions through cooperative reconstruction of the local electronic environment.

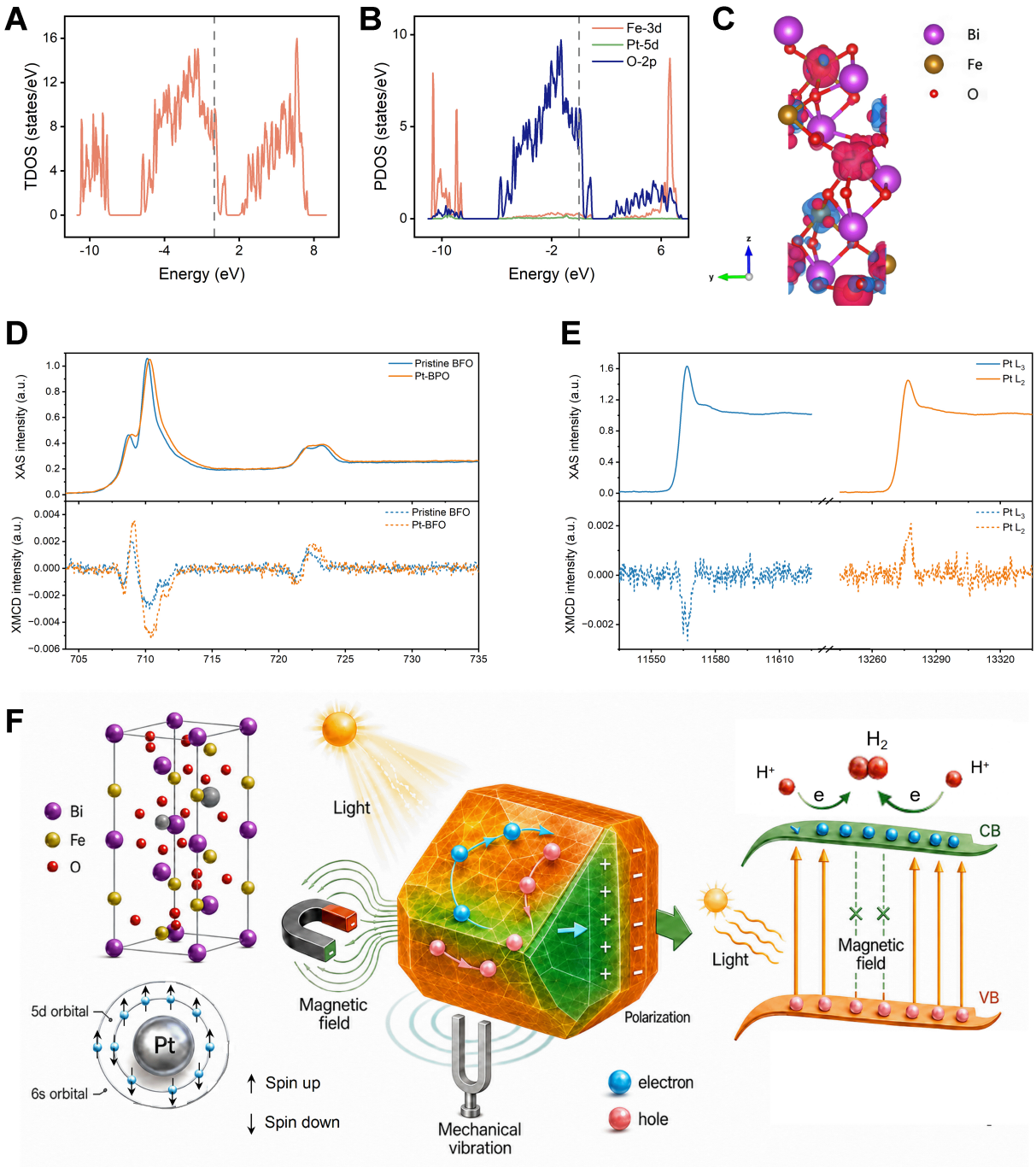


Figure 6. Electronic structure examination and schematic illustration of the multi-field-enhanced photocatalytic pathway of $BiFe(Pt)O_3$: (A) TDOS of $BiFe(Pt)O_3$; (B) PDOS of Fe 3d, Pt 5d, and O 2p orbitals; (C) Charge density distribution of $BiFe(Pt)O_3$; (D) Fe $L_{2,3}$-edge XAS/XMCD spectra of pristine $BiFeO_3$ and $BiFe(Pt)O_3$; (E) Pt $L_{2,3}$-edge XAS/XMCD spectra of $BiFe(Pt)O_3$; (F) Schematic illustration of the synergistic enhancement pathway of photocatalytic hydrogen evolution under the coupling of light irradiation, magnetic field, mechanical vibration, and ferroelectric polarization. TDOS: Total density of states; PDOS: partial density of states; XAS: X-ray absorption spectroscopy; XMCD: X-ray magnetic circular dichroism; CB: conduction band; VB: valence band.

The mechanistic illustration in Figure 6F integrates light irradiation, magnetic field, ferroelectric polarization, and mechanical vibration into a unified multi-field-responsive photocatalytic framework, where orbital reconstruction and spin regulation cooperatively accelerate charge separation, carrier migration, and surface redox reactions. Strong agreement between the electronic-structure calculations and the experimental observations confirms that the reconstructed electronic configuration provides the intrinsic origin of the

multi-field-enhanced hydrogen evolution performance. These results demonstrate that Pt functions as an effective electronic regulator that synchronizes orbital hybridization, spin polarization, and charge redistribution within a unified microscopic mode.

DFT therefore provides the final theoretical verification for the orbital–spin synergistic electronic-state reconstruction proposed in this work. Descriptor-level correlations, electronic-density-of-states examination, charge-density distributions, and the integrated mechanistic model consistently support the same physical picture. Orbital occupation governs electronic hybridization, whereas net spin regulates magnetic interactions and carrier dynamics, and both factors cooperatively optimize the band structure and charge-transfer behavior. Close agreement among computational screening, experimental characterization, explainable deep learning, and first-principles calculations establishes a complete structure–descriptor–electronic-state–performance relationship. This multiscale understanding explains the exceptional photocatalytic hydrogen-evolution performance of $BiFe(Pt)O_3$ and provides a rational strategy for designing high-performance multi-field-responsive photocatalysts through orbital–spin synergistic regulation.

CONCLUSIONS

We demonstrate that orbital–spin synergy governs electronic-state reconstruction in Pt-doped $BiFeO_3$ through the integration of explainable deep learning, first-principles calculations, and experimental validation. Orbital–spin synergy reconstructs the electronic configuration through Pt 5d–Fe 3d–O 2p hybridization and spin redistribution, thereby promoting charge separation, carrier migration, and interfacial redox kinetics under coupled external fields. This work establishes orbital–spin synergy as the fundamental principle of electronic-state engineering and provides a unified descriptor–electronic-state–performance relationship for efficient photocatalytic hydrogen evolution. Pt-doped $BiFeO_3$ is identified by multi-objective DFT screening and experimentally verified to preserve lattice integrity while simultaneously optimizing the electronic structure, ferroelectric polarization, and local chemical environment. Pt-doped $BiFeO_3$ achieves superior photocatalytic hydrogen evolution with prolonged carrier lifetime, reduced charge-transfer resistance, enhanced reactive-species generation, outstanding cycling stability, and remarkable multi-field responsiveness. Strong agreement among computational screening, explainable deep learning, first-principles calculations, and experimental observations demonstrates the reliability and predictive capability of the integrated computational–experimental framework. This strategy offers a more comprehensive route for precise electronic-state regulation than conventional single-property optimization and provides new guidance for rational photocatalyst design toward efficient solar-to-hydrogen energy conversion.

DECLARATIONS

Authors' contributions

Conceptualization: Liu, J.
Investigation: Zhang, W.; Liang, L.; Guan, H.
Data curation: Qiu, P.; Hu, C.; Wu, D.
Writing - original draft: Zhang, W.; Liu, J.
Writing - review and editing: Liu, J.; Fu, C.; Zhang, Q.
Funding acquisition: Liu, J.; Wu, D.

Availability of data and materials

The original contributions presented in this study are included in the article/Supplementary Materials. Further inquiries can be directed to the corresponding author(s).

AI and AI-assisted tools statement

During the preparation of this manuscript, the authors used ChatGPT (Version 5.5) for language editing and grammar correction. In addition, ChatGPT (Version 5.5) was used to assist in generating specific graphical

abstract element, which was subsequently reviewed, edited, and incorporated into the final figure by the authors. These AI tools did not influence the study design, data collection, analysis, interpretation, or the scientific content of the work. All authors take full responsibility for the accuracy, integrity, and final content of the manuscript.

Financial support and sponsorship

This work is financially supported by the Liaoning Applied Fundamental Research Project (Grant No. 2025JH2/101330046) and the Liaoning Provincial Doctoral Startup Fund Project (Grant No. 2025BS0227).

Conflicts of interest

Liang, L. is affiliated with Tangshan Kaicheng Electric Control Equipment Group Co.,Ltd., while the other authors have declared that they have no conflicts of interest.

Ethical approval and consent to participate

Not applicable.

Consent for publication

Not applicable.

Copyright

© The Author(s) 2026.

Supplementary Materials

Supplementary Materials

REFERENCES

1. Jamesh, M.; Tong, H.; Santoso, S. P.; et al. Recent advances in developing nanoscale electro-/photocatalysts for hydrogen production: modification strategies, charge-carrier characterizations, and applications. *Nanoscale* **2024**, *16*, 18213-50. DOI PubMed
2. Xu, F.; Weng, B. Photocatalytic hydrogen production: an overview of new advances in structural tuning strategies. *J. Mater. Chem. A.* **2023**, *11*, 4473-86. DOI
3. Choi, J.; Jung, W.; Gonzalez-Carrero, S.; Durrant, J. R.; Cha, H.; Park, T. Understanding charge carrier dynamics in organic photocatalysts for hydrogen evolution. *Energy. Environ. Sci.* **2024**, *17*, 7999-8018. DOI
4. Rahman, M. Z.; Edvinsson, T.; Gascon, J. Hole utilization in solar hydrogen production. *Nat. Rev. Chem.* **2022**, *6*, 243-58. DOI PubMed
5. Balapure, A.; Ray Dutta, J.; Ganesan, R. Recent advances in semiconductor heterojunctions: a detailed review of the fundamentals of photocatalysis, charge transfer mechanism and materials. *RSC. Appl. Interfaces.* **2024**, *1*, 43-69. DOI
6. Molaei, M. J. Recent advances in hydrogen production through photocatalytic water splitting: a review. *Fuel* **2024**, *365*, 131159. DOI
7. Li, X.; Wang, Q.; Sun, Y.; Sun, S.; Ge, L. Photogenerated charge carriers' regulation strategies: structure design, mechanism, and characterization technology. *Int. J. Hydrogen. Energy.* **2024**, *69*, 1341-65. DOI
8. Chen, T.; Qin, T.; Sun, H.; Su, C. Oxygen vacancy in lead-free perovskite $Cs_2AgBiBr_6/WO_{3-X}$ for enhanced photocatalytic C(sp^3)-H bond oxidation. *Rare. Met.* **2025**, *44*, 6354-65. DOI
9. Li, R.; Luan, J.; Zhang, Y.; et al. A review of efficient photocatalytic water splitting for hydrogen production. *Renew. Sustain. Energy. Rev.* **2024**, *206*, 114863. DOI
10. Pastor, E.; Sachs, M.; Selim, S.; Durrant, J. R.; Bakulin, A. A.; Walsh, A. Electronic defects in metal oxide photocatalysts. *Nat. Rev. Mater.* **2022**, *7*, 503-21. DOI
11. Chen, R.; Ren, Z.; Liang, Y.; et al. Spatiotemporal imaging of charge transfer in photocatalyst particles. *Nature* **2022**, *610*, 296-301. DOI PubMed
12. Dai, B.; Zhou, C.; Yin, H.; Kong, R.; Wang, H.; Xie, Y. Advanced catalysis for efficient hydrogen production. *Microstructures* **2025**, *5*, 2025083. DOI
13. Liu, Q.; Zhan, F.; Luo, H.; et al. Na-Sm bimetallic regulation and band structure engineering in $CaBi_2Nb_2O_9$ to enhance piezo-photocatalytic performance. *Adv. Funct. Mater.* **2023**, *33*, 2303736. DOI
14. Zhang, S.; Yi, X.; Hu, G.; et al. Configuration regulation of active sites by accurate doping inducing self-adapting defect for enhanced photocatalytic applications: a review. *Coord. Chem. Rev.* **2023**, *478*, 214970. DOI

15. Wang, S.; Niu, X.; Wang, L.; Bi, J.; Yang, W.; Hou, H. Recent advances in non-metal doped ZnS nanostructures for photocatalytic hydrogen production. *Microstructures* **2025**, *5*, 2025074. DOI
16. Zhu, C. Z.; Tian, Q. H.; Wang, B. H.; et al. Application of modified cerium dioxide for photocatalytic air pollution purification. *Rare. Met.* **2024**, *43*, 5473-86. DOI
17. Yang, Y.; Toyoda, M.; Yamaguchi, A.; et al. Bandgap widening through doping for improving the photocatalytic oxidation ability of narrow-bandgap semiconductors. *Phys. Chem. Chem. Phys.* **2023**, *25*, 255-61. DOI
18. Ali, S.; Ismail, P. M.; Khan, M.; et al. Charge transfer in TiO_2-based photocatalysis: fundamental mechanisms to material strategies. *Nanoscale* **2024**, *16*, 4352-77. DOI PubMed
19. Lu, J.; Shan, P.; Chen, F.; et al. Construction of a recyclable foam photocatalyst for boosted photothermal-assisted photocatalytic H_2 production. *J. Alloys. Compd.* **2025**, *1014*, 178819. DOI
20. Sui, Q.; Li, R.; Zhang, Y.; et al. High-efficient C_3N_4-viologen charge transfer systems for promoting photocatalytic H_2 evolution through band engineering. *Int. J. Hydrogen. Energy.* **2023**, *48*, 16330-40. DOI
21. Luo, J.; Han, H.; Wu, J.; et al. Excellent photocatalytic activity of MoO_3-adorned g-C_3N_4 systems: construction of S-scheme heterojunction. *Appl. Surf. Sci.* **2022**, *604*, 154512. DOI
22. Yang, M.; Zhan, X. Q.; Ou, D. L.; et al. Efficient visible-light-driven hydrogen production with Ag-doped flower-like $ZnIn_2S_4$microspheres. *Rare. Met.* **2024**, *44*, 1024-41. DOI
23. Lin, R.; Hsueh, C.; Yu, H.; Heine, T.; Chen, C.; Murayama, T. The challenge and opportunity of organic semiconductors in photocatalysis. *Microstructures* **2025**, *5*, 2025071. DOI
24. Wu, B. Y.; Huang, Z. S.; Zhao, D. F.; et al. Computational screening-aided design of transition metal-doped CeO_2 as NH_3-SCR catalysts. *Rare. Met.* **2025**, *44*, 6303-18. DOI
25. Jin, W.; Yang, C.; Pau, R.; et al. Photocatalytic doping of organic semiconductors. *Nature* **2024**, *630*, 96-101. DOI PubMed PMC
26. Guo, Y.; Wen, H.; Guo, Y.; et al. Surface states modulation via vacancy engineering for creating band bending on semiconductor BiOBr photocatalysts. *Colloids. Surf. A. Physicochem. Eng. Asp.* **2024**, *682*, 132915. DOI
27. Zafar, Z.; Yi, S.; Li, J.; et al. Recent development in defects engineered photocatalysts: an overview of the experimental and theoretical strategies. *Energy. Environ. Mater.* **2021**, *5*, 68-114. DOI
28. Wang, J.; Liu, X.; Zheng, H.; et al. Spin-selection in L-chiral Ag-doped WS_2 nanoflower for photocatalysis. *Microstructures* **2026**, *6*, 2026032. DOI
29. Meng, L.; Li, Y.; Zhao, C.; et al. Orbital hybridization-driven singlet oxygen generation in piezo-photocatalytic self-fenton system: synergistic band engineering and spin-state modulation for sustainable water remediation. *Appl. Catal. B. Environ. Energy.* **2025**, *377*, 125521. DOI
30. Liu, Y.; Feng, S.; Yu, J. First-principles study on the electronic structure and photocatalytic properties of transition metal(Fe,Co,Ni) and N co-doped graphene-like ZnO monolayer. *Solid. State. Commun.* **2025**, *404*, 116037. DOI
31. Zhang, F.; Sa, R.; Kong, K.; et al. Electronic configurations modulated by heterometallic orbital interactions of spinel cocatalysts in covalent organic framework-based dyads for photocatalytic hydrogen evolution. *ACS. Catal.* **2026**, *16*, 4868-76. DOI
32. Lv, X.; Ding, X.; Gong, J.; et al. Research progress on rbital hybridization in photocatalysis and electrocatalysis. *Acta. Phys. Chim. Sin.* **2026**, *42*, 100151. DOI
33. Liu, X.; Pu, Y.; Li, Y.; Liu, Z.; Wang, J. Enhanced photocatalytic water splitting via chiral cadmium zinc sulfide nanostructures: spin polarization modulation for efficient charge carrier dynamics. *Solar. RRL.* **2025**, *10*, e202500805. DOI
34. Miao, Y.; Yuan, J.; Zhou, L.; et al. Enhancing hydrogen production from photocatalytic water splitting over $ZnIn_2S_4$/Ni-MOF via magnetically induced spin polarization. *Appl. Catal. B. Environ. Energy.* **2026**, *387*, 126513. DOI
35. Li, Y.; Wang, Z.; Wang, Y.; et al. Local magnetic spin mismatch promoting photocatalytic overall water splitting with exceptional solar-to-hydrogen efficiency. *Energy. Environ. Sci.* **2022**, *15*, 265-77. DOI
36. Wu, Y.; Cheng, L.; Tang, Y.; Sun, H.; Xiang, Q. Unified perspectives on spin polarization in heterogeneous photo/electrocatalysis. *Adv. Funct. Mater.* **2025**, *36*, e16617. DOI
37. Takubo, K.; Ono, A.; Ueno, S.; et al. Photocontrol of ferroelectricity in multiferroic $BiFeO_3$ via structural modification coupled with photocarrier. *Commun. Mater.* **2024**, *5*, 261. DOI
38. Zhang, J.; Zhang, Y.; Li, L.; et al. Synergizing the internal electric field and ferroelectric polarization of the $BiFeO_3/ZnIn_2S_4$ Z-scheme heterojunction for photocatalytic overall water splitting. *J. Mater. Chem. A.* **2023**, *11*, 434-46. DOI
39. Wu, J. Y.; Jin, X.; Wang, J.; et al. Enhancement of photocatalytic activity in $BiFeO_3$ nanoparticles through electrical polarization. *Adv. Energy. Sustain. Res.* **2025**, *6*, 2400285. DOI

40. Ahmad, T.; Jindal, K.; Tomar, M.; Jha, P. K. Effect of codoping of rare earth elements and Cr on multiferroic, optical and photocatalytic properties of $BiFeO_3$. *Mater. Today. Commun.* **2023**, *37*, 107516. DOI
41. Dhawan, A.; Sudhaik, A.; Raizada, P.; et al. $BiFeO_3$-based Z scheme photocatalytic systems: advances, mechanism, and applications. *J. Ind. Eng. Chem.* **2023**, *117*, 1-20. DOI
42. He, J.; Liu, Y.; Qu, J.; Zhang, J.; Fan, F.; Li, C. The ferroelectric effects of rhombohedral and tetragonal $BiFeO_3$ in photoelectrochemical water splitting. *J. Phys. Chem. Lett.* **2024**, *15*, 6031-7. DOI
43. Kumar, M.; Kumar, A.; Sharma, S.; et al. Investigations on low temperature magnetic and magnetoelectric properties of multiferroic-NiO nanocomposites. *J. Alloys. Compd.* **2023**, *965*, 171353. DOI
44. Shah, J. H.; Malik, A. S.; Idris, A. M.; Rasheed, S.; Han, H.; Li, C. Intrinsic photocatalytic water oxidation activity of Mn-doped ferroelectric $BiFeO_3$. *Chin. J. Catal.* **2021**, *42*, 945-52. DOI
45. Wang, Y.; Zheng, L.; Liu, P.; Chen, F.; Chen, R. Tunable photocatalytic and magnetic properties in Y and transition metals (TM = Mn, Co, Ni, Cu, Zn) co-doped $BiFeO_3$: DFT + U study*. *Ferroelectrics* **2023**, *615*, 212-22. DOI
46. Yang, C.; Zhang, Y.; Yue, F.; et al. Co doping regulating electronic structure of Bi_2MoO_6 to construct dual active sites for photocatalytic nitrogen fixation. *Appl. Catal. B. Environ.* **2023**, *338*, 123057. DOI
47. Akarchaou, E. H.; Touti, R.; El, Mekkaouy. A.; Didi, Y.; Tahiri, A.; Chtita, S. Computational analysis of X_2MgTiH_6 (X = Li, Na, and K) double perovskite hydride materials for hydrogen storage applications. *Int. J. Hydrogen. Energy.* **2025**, *161*, 150644. DOI
48. Mohamed Samy, M.; Mekhemer, I. M.; Mohamed, M. G.; et al. Conjugated microporous polymers incorporating Thiazolo[5,4-d]thiazole moieties for Sunlight-Driven hydrogen production from water. *Chem. Eng. J.* **2022**, *446*, 137158. DOI
49. Xia, Y.; Chen, S.; Zhu, X.; Ren, Z.; Feng, W. High-efficiency S-scheme $Bi_4O_5IBr/Bi_5O_7I_{0.7}Br_{0.3}$ double solid solution heterojunction photocatalyst for levofloxacin degradation via optimized carrier dynamics. *Energy. Environ. Mater.* **2026**, *9*, e70204. DOI
50. He, J.; Yue, T.; Kim, Y. L.; Li, Y. High-throughput screening of piezoelectric hybrid organic–inorganic perovskites *via* density-functional theory and machine learning. *J. Mater. Chem. A.* **2026**, *14*, 24610-23. DOI
51. Hu, W.; Zhang, L. High-throughput calculation and machine learning of two-dimensional halide perovskite materials: formation energy and band gap. *Mater. Today. Commun.* **2023**, *35*, 105841. DOI
52. Zhao, G.; Yu, M.; He, C. Theoretical study of nitrate reduction to ammonia on dual-atom doped CoP(101) catalysts. *Surf. Interfaces.* **2025**, *75*, 107859. DOI
53. Zhao, G.; Dai, S.; He, C. Dopant-engineered Ir(100) surfaces for efficient N_2 activation: a combined multi-objective screening and electronic-structure mechanistic study. *Comput. Theor. Chem.* **2026**, *1259*, 115730. DOI
54. Augustine, L. J.; Wang, Y.; Taylor, M. G.; et al. Coupling high-throughput density functional theory, automated experimentation, and adaptive experimental design to achieve selective rare-earth element separations. *J. Am. Chem. Soc.* **2026**, *148*, 40676-87. DOI
55. Su, B. R.; Liu, J. Q.; Zhao, D.; et al. Past, present, prospect: AI-driven evolution of low-dimensional material design for sustainable environmental solutions. *Rare. Met.* **2025**, *44*, 9671-701. DOI
56. Wang, Y.; Zhang, W.; Guan, H.; et al. Interpretable ML-driven high-throughput screening reveals orbital–site–spin synergy for cross-field-enhanced multiferroic perovskite photocatalyst design. *ACS. Catal.* **2026**, *16*, 16994-7010. DOI
57. Song, J.; Wang, S.; Zhang, Z.; Niu, K.; Shan, Y.; Li, Y. Integrated PredRNN++ and phase-field for microstructure prediction and simulation acceleration. *Microstructures* **2026**, *6*, 2026074. DOI
58. Liu, J.; Liang, L.; Su, B.; et al. Transformative strategies in photocatalyst design: merging computational methods and deep learning. *J. Mater. Inf.* **2024**, *4*, 33. DOI
59. Lee, J.; Sun, H.; Liu, Y.; Li, X.; Liu, Y.; Kim, M. State-of-health estimation and anomaly detection in Li-ion batteries based on a novel architecture with machine learning. *Batteries* **2023**, *9*, 264. DOI
60. Fan, T.; Lei, H.; Wang, K.; Qu, B. High-throughput screening of Ni-rich layered cathode materials for sodium-ion batteries based on machine learning. *J. Alloys. Compd.* **2025**, *1026*, 180282. DOI
61. El Fallah, S.; Kharbach, J.; Vanagas, J.; et al. Advanced state of charge estimation using deep neural network, gated recurrent unit, and long short-term memory models for lithium-ion batteries under aging and temperature conditions. *Appl. Sci.* **2024**, *14*, 6648. DOI
62. Islam, S.; Namkoong, G. Interpretable battery SOH prediction: a comparative interpretability framework for multi-architecture ML models. *J. Electrochem. Soc.* **2026**, *173*, 110505. DOI
63. Acharyya, S.; Bhowmick, P. K.; Guha, P. K. Selective identification and quantification of VOCs using metal nanoparticles decorated SnO_2 hollow-spheres based sensor array and machine learning. *J. Alloys. Compd.* **2023**, *968*, 171891. DOI
64. Zafari, M.; Kumar, D.; Umer, M.; Kim, K. S. Machine learning-based high throughput screening for nitrogen fixation on boron-doped single atom catalysts. *J. Mater. Chem. A.* **2020**, *8*, 5209-16. DOI
65. Sheng, Y.; Wu, Y.; Jiang, C.; et al. Interpretable model of dielectric constant for rational design of microwave dielectric materials: a machine learning study. *J. Mater. Inf.* **2025**, *5*, 7. DOI

66. Sahu, N.; Azad, C.; Kumar, U. Study and prediction of photocurrent density with external validation using machine learning models. *Int. J. Hydrogen. Energy.* **2024**, *92*, 1335-55. DOI
67. Wei, M.; Chen, Y.; Bi, Y.; et al. Degradation-informed closed-loop feature optimization and SHAP-enhanced machine learning for lithium-ion battery SOH estimation. *J. Power. Sources.* **2026**, *689*, 240784. DOI
68. Li, X.; Zhang, H.; Wang, C.; et al. Accelerated design of 5xxx-Series Al-Mg alloys with enhanced mechanical properties via interpretable machine learning and microstructural validation. *J. Alloys. Compd.* **2026**, *1050*, 185653. DOI
69. Xing, X.; Feng, H.; Kuang, Y.; Zhang, J.; Yu, Y.; Chen, C. Interpretable machine-learning modeling of corrosion rates of casing and tubing materials under high-temperature and high-pressure downhole conditions. *Int. J. Electrochem. Sci.* **2026**, *21*, 101377. DOI

Disclaimer/Publisher's Note: All statements, opinions, and data contained in this publication are solely those of the individual author(s) and contributor(s) and do not necessarily reflect those of OAE and/or the editor(s). OAE and/or the editor(s) disclaim any responsibility for harm to persons or property resulting from the use of any ideas, methods, instructions, or products mentioned in the content.


© The Author(s) 2026. Open Access This article is licensed under a Creative Commons Attribution 4.0 International License (https://creativecommons.org/licenses/by/4.0/), which permits unrestricted use, sharing, adaptation, distribution and reproduction in any medium or format, for any purpose, even commercially, as long as you give appropriate credit to the original author(s) and the source, provide a link to the Creative Commons license, and indicate if changes were made.